Fuel 317 (2022) 123420

Contents lists available at ScienceDirect

Fuel

journal homepage: www.elsevier.com/locate/fuel

Full Length Article

Integrated CO_2 capture and methanation on Ru/CeO_2-MgO combined materials: Morphology effect from CeO_2 support

Shuzhuang Sun [a], Hongman Sun [a], Shaoliang Guan [b,c], Shaojun Xu [b,d,*], Chunfei Wu [a,*]

[a] School of Chemistry and Chemical Engineering, Queen's University Belfast, Belfast BT7 1NN, UK
[b] Cardiff Catalysis Institute, School of Chemistry, Cardiff University, Cardiff CF10 3AT, UK
[c] Harwell XPS, Research Complex at Harwell, Rutherford Appleton Laboratory, Didcot OX11 0FA, UK
[d] UK Catalysis Hub, Research Complex at Harwell, Didcot OX11 0FA, UK

ARTICLE INFO

Keywords:
Morphology dependent
Integrated CO_2 capture and methanation
Combined materials
Ru/CeO_2-MgO
In situ DRIFTS

ABSTRACT

Integrated CO_2 capture and methanation (ICCM) is attracting more attention to promote the reduction of CO_2 emission. This work developed and applied a set of combined materials using Ru/CeO_2 as catalyst and physically mixed Li, Na, K-doped MgO as adsorbent for the ICCM process. The influences of morphologies of CeO_2 (rod, particle, and cube) in combined materials are investigated explicitly in terms of CO_2 conversion and CH_4 yield. Compared to the CeO_2 with cube morphology, the CeO_2 with rod and particle morphologies showed better Ru dispersion and more abundant support-metal interaction (SMI). The combined materials with rod and particle morphologies CeO_2 (Ru/rod-CeO_2-MgO and Ru/particle-CeO_2-MgO) show more superior catalytic performance (0.33 and 0.29 mmol/g for CH_4 yield and 55.7% and 59.8% for CO_2 conversion, respectively) than that with Ru/cube-CeO_2-MgO. Furthermore, the Ru/rod-CeO_2-MgO shows excellent catalytic stability and reusability during 9 cyclic ICCM evaluations. In situ DRIFTS of Ru/CeO_2-MgO revealed that the formates and dissociated CO_2 (Ru-CO) might be the critical methanation intermediates in ICCM.

1. Introduction

Global warming and the related severe climate issues caused by the continuous rise of carbon dioxide (CO_2) emissions have attracted significant attention [1]. CO_2 capture and utilization (CCU) is a promising solution to reduce the emission of CO_2 and can be closely integrated with current industrial processes (such as power plants and cement manufacturing). Therefore, extensive researches have been carried out on developing sorbents for carbon capture [2] and catalysts for CO_2 conversion such as CO_2 methanation [3–4], reverse-water–gas shift reaction [5–7], dry reforming of methane [8,9], etc. However, the energy consumption on CO_2 separation, enrichment and transportation significantly increase the overall cost of the CCU process.

Recently, integrated CO_2 capture and utilization (ICCU) using dual-functional combined materials is gaining increasing interest by combining CO_2 adsorption and utilization in a single reaction system [10–12]. ICCU is a gas-swing two-stage system, as shown in Fig. 1. The 1st stage is the CO_2 capture from the diluted CO_2 exhaust gas, and the 2nd stage is CO_2 conversion accompanied by the recovery of adsorbents. It is suggested that ICCU has lower energy consumption benefited from the isothermal operating condition and less capital investment on the process units compared with conventional CCU [13]. The key point is that ICCU avoids CO_2 enrichment and transportation steps by in situ converting the fixed CO_2, thus greatly reducing the cost of CCU.

CO_2 methanation, believed as a promising process to recycle CO_2 back to fuel, was applied in the 2nd stage of ICCU in this work. Owing to its exothermic property, CO_2 methanation prefers a moderate reaction temperature (<500 °C). Nobal metal-based catalysts (e.g. Ru [3,14], Au [15], and Pd [16]) have been widely used to achieve excellent catalytic performance owing to their outstanding catalytic activity and CH_4 selectivity. Furthermore, it is well known that the interaction between active metals and supports plays a vital role in catalytic processes [15,17], especially for catalysts with reducible supports (e.g. CeO_2 [18,19], TiO_2 [20,21], etc.). The CeO_2 has been widely utilized in various applications, such as biotechnology [22], catalysis [23–25], sensor [26], sorbents [27], etc. Recent studies speculated that the Support-Metal Interaction (SMI) and oxygen vacancies on catalysts are highly relevant to their catalytic performance [28–31]. The

* Corresponding authors at: Cardiff Catalysis Institute, School of Chemistry, Cardiff University, Cardiff CF10 3AT, UK (S. Xu). School of Chemistry and Chemical Engineering, Queen's University Belfast, Belfast BT7 1NN, UK (C. Wu).
E-mail addresses: xus25@cardiff.ac.uk (S. Xu), c.wu@qub.ac.uk (C. Wu).

https://doi.org/10.1016/j.fuel.2022.123420
Received 30 September 2021; Received in revised form 12 January 2022; Accepted 22 January 2022
Available online 1 February 2022
0016-2361/© 2022 The Authors. Published by Elsevier Ltd. This is an open access article under the CC BY license (http://creativecommons.org/licenses/by/4.0/).

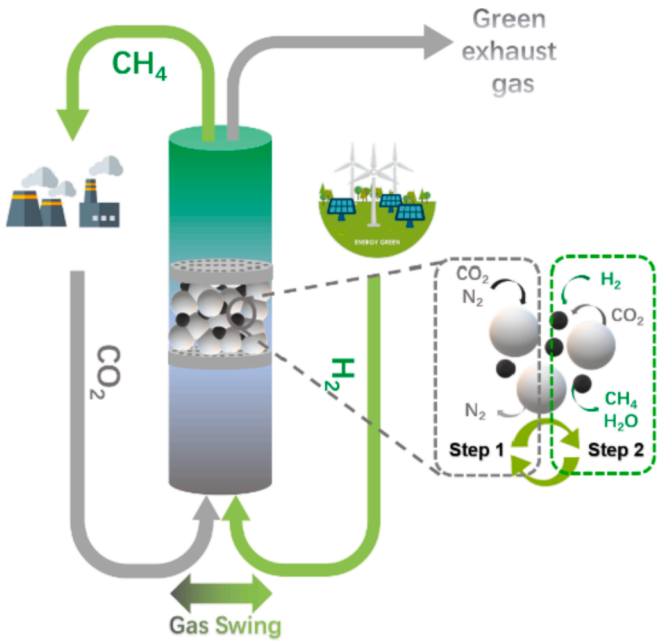

Fig. 1. Schematic diagram of integrated CO_2 capture and methanation process.

morphologies of supports [32] and the preparation method of catalysts [33] have influences on SMI and oxygen vacancies of supported catalysts, and have been widely studied in terms of the catalytic role of SMI and oxygen vacancy [24,34–36]. Furthermore, the electron transfer between reducible supports and metals is also considered to be important to CO_2 methanation performance (i.e. CH_4 selectivity) [32,37]. As a novel process, the integrated CO_2 capture and methanation (ICCM) has a different catalytic environment from that of traditional CO_2 methanation. And the effect of CeO_2 morphology on the ICCM process worth a comprehensive assessment in realtion to CO_2 adsorption and the following catalytic methanation.

$$CO_2 + 4H_2 = CH_4 + 2H_2O \Delta H_{298K} = -252.9 kJ/mol \quad (1)$$

The ICCM process includes the steps of CO_2 adsorption, product desorption, and the corresponding diffusion of chemicals [16], and requires optimized temperatures to balance these processes and maintain better kinetics and thermodynamics. However, there are few choices of adsorbents that are suitable for moderate-temperature (200–500 °C) CO_2 capture applications. In the previous research, we utilized Li, Na, K-doped MgO as CO_2 adsorbent and achieved acceptable capture performance at 300 °C [38,39], which matches the CO_2 methanation requirement. For the controlled component of catalysts, Ru is selected as the effective catalytic active metal for CO_2 methanation [14,40–42].

Herein, a set of combined materials using Ru/CeO_2 as a catalyst and physical mixed MgO as adsorbent were developed with three different CeO_2 morphologies, including rod, particle, and cube CeO_2, to investigate the effect of CeO_2 support morphology on the ICCM process. In particular, we studied the influence of ceria support on the morphologies, reducibility, SMI and oxygen vacancies of Ru/CeO_2, in relation to CO_2 adsorption and CH_4 production. Furthermore, we investigated the mechanism of ICCM over Ru/CeO_2-MgO by in situ DRIFTS and proposed the ICCM reaction pathways.

2. Experimental section

2.1. Materials preparation

2.1.1. Preparation of CeO_2 supports with different morphologies

Three different CeO_2 supports with the rod, particle, and cube morphologies were produced. The CeO_2 supports with rod and cube morphologies were prepared by a hydrothermal method [18,43]. Typically, 5.21 g $Ce(NO_3)_3{\cdot}6H_2O$ (>99%, Sigma-Aldrich) was dissolved in deionized water (30 ml) to produce a Ce source solution, and 57.6 g NaOH (>95%, Sigma-Aldrich) was dissolved in deionized water (210 ml) followed by mixing the Ce source solution with NaOH solution to obtain a slurry. After stirring 30 mins at room temperature, the slurry was transferred into Teflon-lined stainless-steel autoclaves and held at 100 and 200 °C for 24 h to obtain rod-CeO_2 and cube-CeO_2 supports, respectively. After the autoclave was cooled to room temperature naturally, the precipitates were separated by vacuum filtration, washed by deionized water and ethanal to neutrality, and dried at 100 °C in air overnight. Particle-CeO_2 was prepared by precipitating ammonia cerium nitrate with urea in an aqueous solution, as reported by Tana et al. [44]. Typically, 60 g of $(NH_4)_2Ce(NO_3)_6$ (>99%, Sigma-Aldrich) and 200 g of urea (>99%, Sigma-Aldrich) were dissolved into 2000 ml distilled water, and the mixture was heated to 90 °C under stirring and kept at this temperature for 27 h. After filtration and washing with water, the precipitate was dried at 100 °C overnight. All three dried materials were calcined at 600 °C for 5 h with a heating rate of 5 °C min^{-1} to obtain CeO_2 supports with various morphologies, donated as rod-CeO_2, particle-CeO_2, and cube-CeO_2, respectively.

2.1.2. Preparation of Ru/CeO_2 materials

The Ru/CeO_2 catalysts with 2 wt% Ru was prepared using a wet impregnation method. In general, 1.0 g of CeO_2 powder (rod-CeO_2, particle-CeO_2, or cube-CeO_2) was suspended in 20 ml of Ru^{3+} solution ($RuCl_3$, 0.01 mol/L) followed by stirring for 24 h at room temperature. The suspension was evaporated and dried at 110 °C overnight and then calcined in air at 300 °C for 2 h with a heating rate of 2 °C min^{-1}, donated as Ru/rod-CeO_2, Ru/particle-CeO_2 and Ru/cube-CeO_2. The samples were reduced in 5% H_2/N_2 at a flow rate of 50 ml min^{-1} at 300 °C for 3 h (heating rate is 2 °C min^{-1}) to obtain the reduced Ru/CeO_2 catalysts.

2.1.3. Preparation of dual functional combined materials

The Li, Na, K-doped MgO adsorbent was prepared using a method reported by Harada et al. [38]. Firstly, 9.713 g $4MgCO_3{\cdot}Mg(OH)_2{\cdot}5H_2O$ (>99%, Sigma-Aldrich), 0.207 g $LiNO_3$ (>99%, Sigma-Aldrich), 0.153 g $NaNO_3$ (>99%, Sigma-Aldrich), and 0.526 g KNO_3 (>99%, Sigma-Aldrich) were added into 40 ml deionized water with stirring at room temperature for 60 min. The obtained white slurry was dried at 110 °C overnight and then calcined at 450 °C for 4 h. The combined materials were prepared by physically mixing the Li, Na, K-doped MgO sorbent and the reduced Ru/CeO_2 catalysts in a mortar with a 2:1 mass ratio. The obtained combined materials were donated as Ru/rod-CeO_2-MgO, Ru/particle-CeO_2-MgO, and Ru/cube-CeO_2-MgO, respectively.

2.2. Materials characterization

The elemental analysis of Ru/CeO_2 catalysts was carried out using inductively coupled plasma-optical emission spectroscopy (ICP-OES). The samples were digested by peroxide fusion and then tested by Perkin Elmer PE2400CHNS. Powder X-ray diffraction (PXRD) of all catalysts was measured on a PANalytical Empyrean series 2 diffractometer with Cu Kα X-ray source. And the Scherrer's equation was used to calculate the average crystallite size of different Ru/CeO_2 samples. Transmission electron microscopy (TEM) was obtained using a JEOL 2100 observing the morphologies and Ru dispersion of reduced Ru/CeO_2.

X-ray photoelectron spectrum (XPS) analysis of Ru/CeO_2 materials was performed using a Thermo Fisher Scientific NEXSA spectrometer fitted with a mono-chromated Al Kα X-ray source (1486.7 eV). The Ru/CeO_2 materials were reduced at 300 °C for 3 h in 5% H_2/N_2 and then protected by Ar in a glove box before XPS analysis to prevent the re-oxidation of oxygen vacancies and reduced Ru in air. Data were recorded at pass energies of 200 eV for survey scans and 50 eV for the high-resolution scan with 1 eV and 0.1 eV step sizes, respectively, at a spot

size of approximately 400 μm. The charge neutralization of the sample was achieved using a combination of both low-energy electrons and argon ions. C 1 s electron at 284.8 eV was used as a standard reference to calibrate the photoelectron energy shift. All the data analysis was performed on the Casa XPS software (version: 2.3.22PR1.0).

H_2 temperature-programmed reduction (H_2-TPR) was performed by Hi-Res TGA 2950 thermogravimetric analyzer to characterize the reducibility of the Ru/CeO_2 materials. Typically, the samples were pre-treated under N_2 at 600 °C for 10 mins and then equilibrated at 50 °C in N_2 followed by raising the temperature to 800 °C at a rate of 10 °C min^{-1} in 100 ml/min 5% H_2/N_2.

2.3. Integrated CO_2 capture and methanation (ICCM) evaluation

The ICCM performances of Ru/CeO_2-MgO combined materials with different CeO_2 morphologies were carried out in a fixed bed reactor with a stainless-steel tube (8 mm in diameter) at atmospheric pressure. Typically, 0.3 g combined materials was placed in the middle of the reaction tube and fixed by quartz wool, and two thermocouples were used to control the temperature of the combined materials and the furnace, respectively. Omega mass flow meter controllers (FMA-A2306) were calibrated by a bubble flowmeter and used to control the gas flow. ICCM includes two stages: carbonation reaction (1st stage) and CO_2 methanation (2nd stage). The 1st stage was performed using 35% CO_2/N_2 at 100 ml/min at 300 °C for 1 h, followed by sample purge in 50 ml min^{-1} N_2 for 10 min. Then, 5% H_2/N_2 at a 50 ml min^{-1} flow rate was switched on for the 2nd stage for 30 min isothermally. The exhaust gases coming out of the 2nd stage reactor were collected by a gasbag and analyzed by a GC (HP Hewlett 5890 series II gas chromatograph) with a Restek Shincarbon ST 100/120 column (2 m, 1 mm ID/1/16'' OD Silco). The cycle evaluation was performed with extra 20 mins N_2 purge among each cycle. The yields of CH_4, CO_2, and CO_2 conversion were calculated using the below equations (No CO and other hydrocarbons were detected):

$$Y_{CH_4} = \frac{V_{gas} * F_{CH_4}}{22.4 * m_{DFM}} \quad (2)$$

$$Y_{CO_2} = \frac{V_{gas} * F_{CO_2}}{22.4 * m_{DFM}} \quad (3)$$

$$C_{CO_2} = \frac{Y_{CH_4}}{(Y_{CO_2} + Y_{CH_4})} * \% \quad (4)$$

Y_{CH4} *(mmol* g^{-1}*)*, Y_{CO2} *(mmol* g^{-1}*)* and C_{CO2} *(%)* represent CH_4 yield (mmol CH_4 per gram of combined materials), CO_2 yield (mmol CO_2 per gram of combined materials) and CO_2 conversion, respectively. V_{gas} and F are the produced gas volume of exhaust gas *(ml)* and gas fraction *(%)* determined from GC, respectively.

2.4. In situ DRIFTS (diffused reflectance infrared fourier transform spectroscopy) study

The in situ DRIFTS tests of ICCM over Ru/rod-CeO_2 and Ru/rod-CeO_2-MgO were carried out using an Agilent Cary 680 FTIR spectrometer with a liquid N_2 cooled detector. The spectra were recorded with 4 cm^{-1} resolution, and each spectrum was averaged 128 times. The experimental setup is as follows: The catalysts were pre-treated with He (99.999%, BOC gas Ltd.) at 150 °C for 10 mins to remove the surface adsorbates and then increase the temperature to reaction temperature of 300 °C. Then H_2 (5% H_2/N_2) was introduced to reduce catalysts for 2 h. Then switch gas flow to He to remove the residual H_2 for 10 min and collect the background reference signal. The carbonation step was carried out using 35% CO_2/N_2 for 60 mins; the purge step proceeded with He for 9 mins to remove the gas phase CO_2; followed with the regeneration step, which was carried out by switching gas flow to 5% H_2/N_2 for 60 mins. The ICCM of Ru/rod-CeO_2 and Ru/rod-CeO_2-MgO (carbonation-purge-hydrogenation) was tested at 300 °C under atmospheric pressure.

3. Results and discussion

3.1. Characterization of Ru/CeO_2 materials

To investigate the effect of CeO_2 morphologies on ICCM, Ru loading on CeO_2 supports is 1.9% ± 0.13% (Table 1). Fig. 2a shows the XRD patterns of the reduced Ru/CeO_2 catalysts with different CeO_2 morphologies, referring to the standard peak position of hcp-structured Ru (JCPDS 06-0663), tetragonal RuO_2 (JCPDS 40-1290), and cubic-structured CeO_2 (JCPDS 34-0394), respectively. The peaks at 2 Theta of 28.8°, 33.3°, 47.7°, 56.6°, 59.4°, 69.6°, and 76.9° are derived from the CeO_2 lattice plane of (111), (200), (220), (311), (222), (400), and (331) [19,45], respectively. Furthermore, the average crystallite size of CeO_2 in Ru/CeO_2 materials is calculated using the Scherrer equation as 9.0, 6.9, and 53.9 nm for Ru/rod-CeO_2, Ru/particle-CeO_2 and Ru/cube-CeO_2, respectively. Smaller supports crystallite size is more helpful to disperse Ru. There is only one small peak of Ru (2 Theta = 44°) observed in the Ru/cube-CeO_2 sample and no observation on Ru/rod-CeO_2 and Ru/particle-CeO_2, indicating that Ru has better dispersion on the rod and particle CeO_2 supports.

The morphologies of the Ru/CeO_2 catalysts were determined using Transmission electron microscopy (TEM). As shown in Fig. 3a and 3b, the Ru/rod-CeO_2 catalyst exhibits a morphology of rod with a uniform diameter (8–10 nm) and length from 20 to 200 nm. Ru/particle-CeO_2 (Fig. 3d and e) and Ru/cube-CeO_2 (Fig. 3g and h) show uniform particle shapes (5–10 nm) and cubic structure (10–50 nm), respectively. The particle size of CeO_2 in various Ru/CeO_2 materials is consistent with the average size calculated from XRD (Table 1). It is noted that all the three CeO_2 supports show a lattice spacing of 0.31 nm, which is assigned to the (111) lattice plane [30]. The high temperature calcination (600 °C) may induce the uniform crystal lattice. Furthermore, smaller CeO_2 supports particles are suggested to benefit the dispersion of metals, in which the rod-CeO_2 and particle-CeO_2 possess much better Ru dispersion (Fig. 3c, 3f and 3i). The Ru clusters (1–2 nm) on the surface of cube-CeO_2 are much larger, which is consistent with XRD observation (Fig. 2a).

Fig. 2b and 2c illustrate the porosity and pore size distributions of Ru/CeO_2 materials. All three materials show typical type IV isotherms with distinct hysteresis loops. In particular, Ru/rod-CeO_2 and Ru/cube-CeO_2 exhibit type H3 hysteresis loops, indicating the existence of slit-shaped pores in rod-CeO_2 and cube-CeO_2, while Ru/particle-CeO_2 possesses type H2 hysteresis loops owing to the irregular pores in the particle aggregates. Furthermore, the Ru/particle-CeO_2 possesses highest specific surface area (114.0 m^2 g^{-1}) followed with Ru/rod-CeO_2 (90.2 m^2 g^{-1}) and Ru/cube-CeO_2 (26.7 m^2 g^{-1}). The rod-CeO_2 and particle-CeO_2 samples contribute to better Ru metal dispersion by providing more surface, which is consistent with the results of TEM and XRD.

Table 1
Elemental analysis, average crystallite size, surface area, and pore volume of Ru/CeO_2 materials.

Sample	Ru content [a](wt. %)	CeO_2 [b] (nm)	S_{BET} [c] (m^2g^{-1})	V_p [d] (cm^3g^{-1})
Ru/rod-CeO_2	1.8	9.0	90.2	0.33
Ru/particle-CeO_2	2.0	6.9	114.0	0.23
Ru/cube-CeO_2	1.8	53.9	18.0	0.12

[a] Element percentage evaluated by elemental analysis.
[b] Average crystallite size obtained from Scherrer's equation (220 plane at 2 Theta = 47.7° was applied to calculated the crystal size).
[c] Multipoint BET surface area.
[d] BJH method cumulative desorption pore volume.

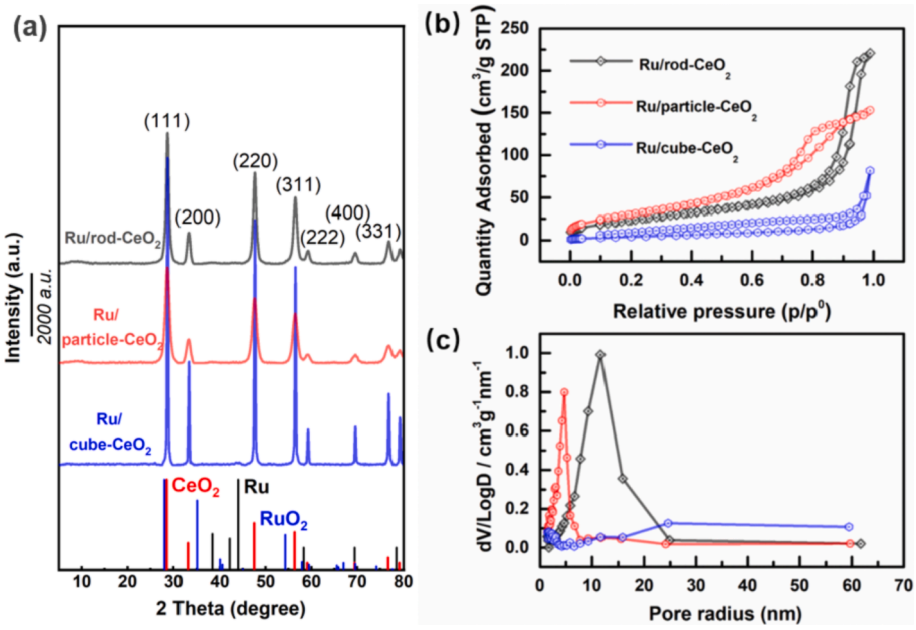

Fig. 2. (a) XRD patterns of reduced Ru/CeO_2 materials with different CeO_2 morphologies; (b) N_2 adsorption–desorption isotherms and (c) Pore size distribution of Ru/CeO_2 materials (BJH desorption branch).

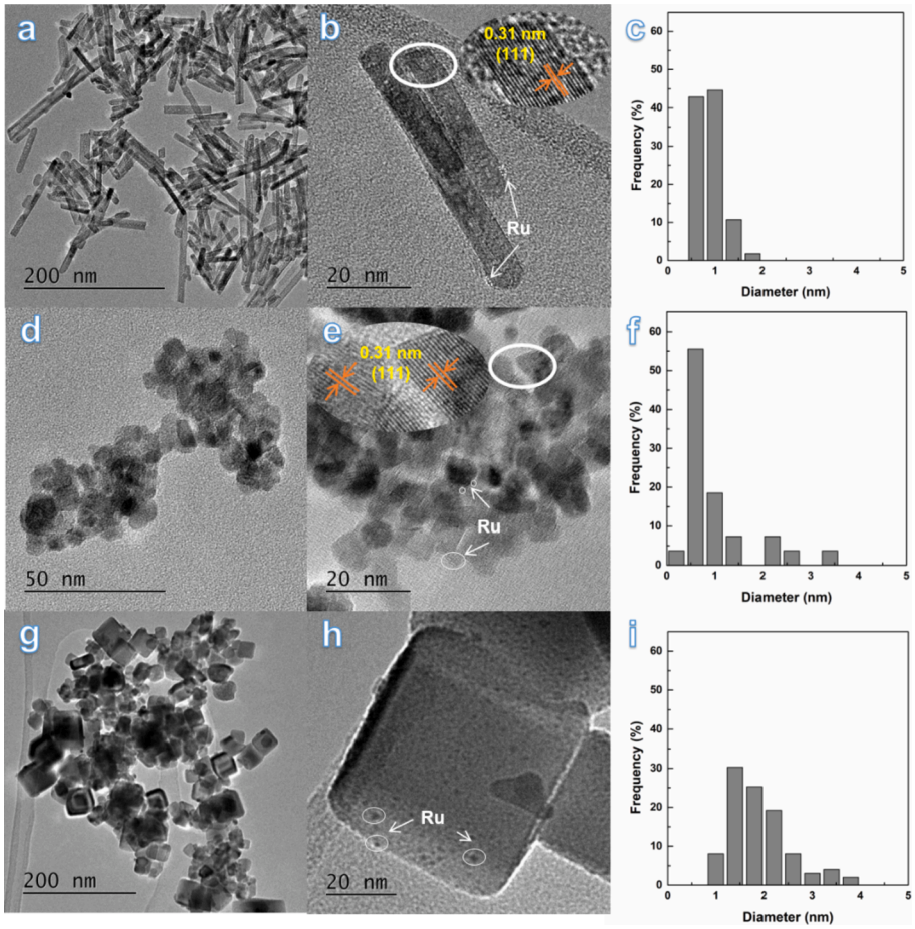

Fig. 3. TEM images and Ru size distribution of 2 wt% reduced $Ru/rod\text{-}CeO_2$ (a, b and c), $Ru/particle\text{-}CeO_2$ (d, e and f) and $Ru/cube\text{-}CeO_2$ (g, h and i).

3.2. Support-metal interaction and oxygen vacancies of Ru/CeO_2 materials

To understand the effect of CeO_2 morphology on supported Ru species, the reducibility of Ru/CeO_2 materials was investigated using H_2 temperature-programmed reduction (H_2-TPR). As shown in Fig. 4, two distinct peaks are observed at 110–160 °C (peak α) and 170–190 °C (peak β), which are related to the reduction of RuO_x species [39]. It is believed that RuO_x species with reduction peaks at a lower temperature (peak α) are related to smaller particle size accomplished with Ru-O-Ce bonds [45–46]. In contrast, the bigger RuO_x clusters, which are composed of Ru-O-Ru bonds [47], needs higher reduction temperature (peak β) [45]. Ru/rod-CeO_2 shows more significant peak α with lower reduction temperature (118 °C) than Ru/particle-CeO_2 (158 °C) and Ru/cube-CeO_2 (160 °C), indicating more abundant SMI (Ru-O-Ce species). It is noted that all Ru/CeO_2 materials can be thoroughly reduced before 200 °C, indicating the metallic state Ru at ICCM evaluation condition.

The SMI and oxygen vacancies on reducible supports (CeO_2, TiO_2, etc.) play key roles in catalytic reactions [43,48]. Therefore, X-ray photoelectron spectrum (XPS) analysis (Fig. 5) was carried out to obtain further insight into the metal states and oxygen vacancies on the Ru/CeO_2 materials. The valences of Ru are assigned to the peaks of Ru $3d_{3/2}$ and Ru $3d_{5/2}$ (Fig. 5a), which are composed of metallic stated Ru^0 (around 280.4 eV and 284.6 eV) and compound stated $Ru^{\delta+}$ (around 281.7 eV and 285.8 eV). $Ru^{\delta+}$ in Ru/CeO_2 is attributed to the SMI or Ru diffusion in CeO_2 lattice [48], and the ratio of $Ru^{\delta+}/(Ru^0 + Ru^{\delta+})$ (Table 2) can be used to semi-quantify SMI [49–50]. Ru/rod-CeO_2 shows the highest $Ru^{\delta+}/(Ru^0 + Ru^{\delta+})$, suggesting the most abundant SMI and well-dispersed Ru, consistent with H_2-TPR results (Fig. 4). Furthermore, an enhanced Ru valence state is believed to facilitate the dissociation of CO_2 into CO [37], which is a pivotal intermediate step of CO_2 methanation.

The peaks of Ce 3d are deconvoluted to analyze the valence state of Ce (Ce^{3+} and Ce^{4+}). Ten peaks constitute two series of spin–orbit lines u and v. Four of the peaks are located at 880.9 eV (v_0), 884.6 eV (v'), 898.7 eV (u_0) and 902.7 eV (u'), which belong to Ce^{3+}, while the other six peaks belong to Ce^{4+} [10]. The presence of Ce^{3+} is related to oxygen vacancies [39], surface OH groups or carbonate species [43]. As shown in Table 2, the Ru/cube-CeO_2 catalyst has the highest Ce^{3+}/Ce^{4+} ratio (0.35), followed by the Ru/particle-CeO_2 (0.28) and Ru/rod-CeO_2 (0.27) catalysts.

The O 1s XPS spectra of Ru/CeO_2 is shown in Fig. 5c. The peaks at around 529.4 eV and 530.9 eV are assigned to the lattice oxygen (O_L) and oxygen vacancies (O_V), respectively [48]. The oxygen vacancies could be ascribed to metal doping [51] or the support materials defects [52]. The ratio of O_V/O_L (Table 2) could represent the abundance of oxygen vacancy on CeO_2. The results show that the Ru/cube-CeO_2 catalyst has the most abundant oxygen vacancy defects compared with the other two catalysts, which is consistent with the analysis of Ce 3d. These oxygen vacancies can promote CO_2 adsorption by forming bicarbonates [53], and might improve the conversion of CO_2 [54].

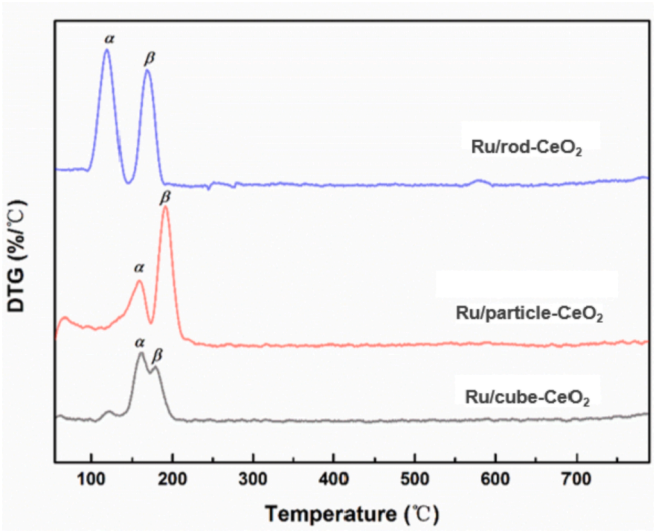

Fig. 4. H_2-TPR profiles of Ru/CeO_2 with different CeO_2 morphologies.

In summary, Ru/rod-CeO_2 shows the most abundant SMI and highest Ru valence (Fig. 4). On the contrary, Ru/cube-CeO_2 possesses more oxygen vacancies. However, it disperses Ru poorer and has the lowest Ru valence.

3.3. Evaluation of integrated CO_2 capture and methanation (ICCM) on Ru/CeO_2-MgO combined materials

The ICCM process is a combination of several steps, including CO_2 capture over the physical mixed Li, Na, K-doped MgO (Eq.5), the purge of residual CO_2, and CO_2 methanation accompanied with the regeneration of adsorbents (Eqs. (1) and (6)).

$$CO_2 + MgO \leftrightarrow MgCO_3 \tag{5}$$

$$4H_2 + MgCO_3 = MgO + CH_4 + 2H_2O \tag{6}$$

The performances of ICCM over Ru/CeO_2-MgO with different CeO_2 morphologies are shown in Fig. 6. Owing to the partial desorption of CO_2 from the adsorbent, the following analysis focuses on the desorbed one-carbon (C1) species (CO_2 and CH_4) in the 2nd stage. The desorption capacity of C1 species over combined materials, representing the CO_2 throughput, was evaluated using the sum of CO_2 and CH_4 yield. All the detected C1 species come from the adsorbed CO_2 in the 1st stage of ICCM. The order of C1 species desorption capacity is Ru/particle-CeO_2-MgO (0.49 mmol/g_{DFM}) < Ru/rod-CeO_2-MgO (0.60 mmol/g_{DFM}) < Ru/cube-CeO_2-MgO (1.29 mmol/g_{DFM}), as shown in Fig. 6. Furthermore, there are significant carbonate peaks on the spent combined materials of Ru/cube-CeO_2-MgO (Fig. 7) after releasing the most abundant C1 species, indicating its enhanced CO_2 adsorption compared to the other two materials.

On the contrary, there is no distinct carbonates peak of spent Ru/rod-CeO_2-MgO and Ru/particle-CeO_2-MgO, representing the sufficient regeneration of MgO after the hydrogenation step. It is speculated that the differences in CO_2 adsorption over the three Ru/CeO_2-MgO combined materials are related to the different amounts of oxygen vacancies on the surface of CeO_2 with different morphologies. Compared to the rod and particle-CeO_2, the higher oxygen vacancies on the surface of cube-CeO_2 might benefit the formation of bicarbonates [53] to enhance the CO_2 adsorption capacity of combined materials.

However, oxygen vacancies cannot significantly improve the catalytic methanation in ICCM. For example, higher CO_2 conversion was achieved using the combined materials of Ru/rod-CeO_2-MgO (55.7%) and Ru/particle-CeO_2-MgO (59.8%) compared to Ru/cube-CeO_2-MgO (2.7%). It is concluded that better Ru dispersion and SMI promote the catalytic performance of CO_2 utilization. Furthermore, there is no CO generation in ICCM over Ru/CeO_2-MgO owing to the excellent CH_4 selectivity of Ru. The limited hydrogen spillover from Ru metals to supports might also contribute to high CH_4 selectivity [32].

Several factors contribute to the significantly improved CO_2 conversion and CH_4 yield of Ru/rod-CeO_2-MgO and Ru/particle-CeO_2-MgO. (1) The better dispersion of Ru (indicated from TEM analysis, Fig. 3) on rod-CeO_2 and particle-CeO_2 can increase the reactant contact with the Ru active sites. (2) The higher BET surface area could facilitate the accessibility of active sites. (3) The abundant interaction between Ru active metals and CeO_2 supports [17,55] can act as the center of catalytic activities. (4) The abundant oxygen vacancies would lead to the enhanced CO_2 absorption performance. Therefore, It is suggested that the optimal composition of the combined materials with CeO_2 as support is to have abundant SMIs with a well-dispersed active metal site, while

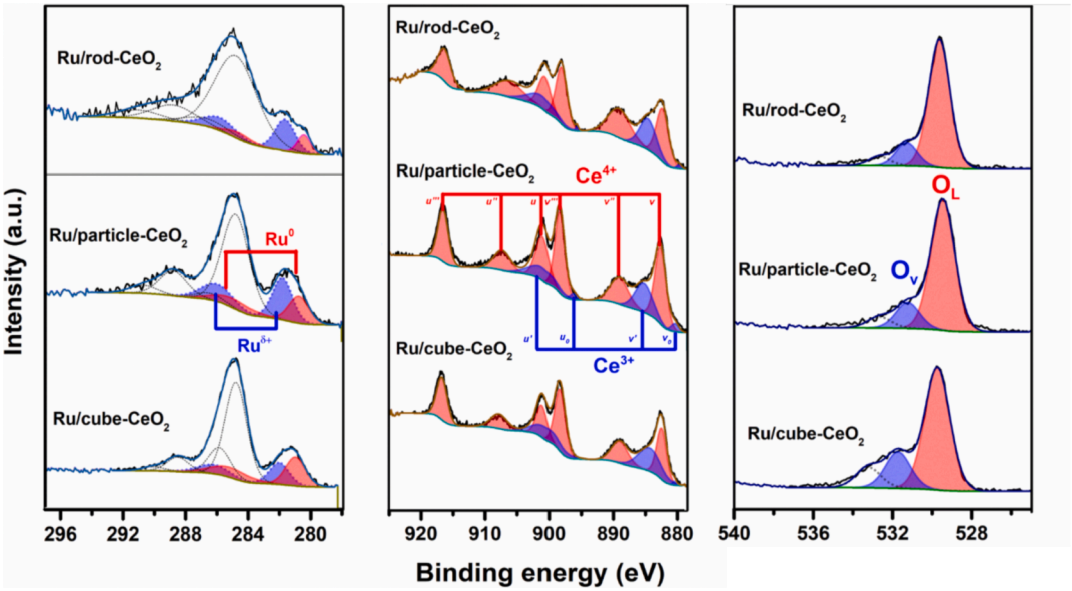

Fig. 5. XPS spectra with fitting peaks of Ru 3d (a), Ce 3d (b), O 1 s (c) of reduced Ru/CeO_2 with different CeO_2 morphologies.

Table 2
XPS results of Ru/CeO_2 with different CeO_2 morphologies.

Sample	Ru 3d $Ru^{\delta+}/(Ru^0 + Ru^{\delta+})$	Ce 3d Ce^{3+}/Ce^{4+}	O 1s O_V/O_L
Ru/rod-CeO_2	0.71	0.27	0.18
Ru/particle-CeO_2	0.61	0.28	0.20
Ru/cube-CeO_2	0.43	0.35	0.30

the adjustment of oxygen vacancies is more related to the CO_2 capacity in ICCM.

The catalytic stability and reusability of Ru/rod-CeO_2-MgO combined materials in ICCM were also investigated in this work. As shown in Fig. 8, it is interesting that the capacity of CO_2 desorption decreases from 58.5 to 5.3 μmol/g_{DFM} after 9 cycles, whilst the CH_4 yield only decrease ~ 20% (from 0.34 to 0.27 mmol/g_{DFM}). Furthermore, the catalytic performance of Ru/rod-CeO_2-MgO for ICCM stabilizes after 5 cycles with > 95% CO_2 conversion using 5% H_2/N_2, which outperforms the state-of-the-art conventional CO_2 methanation (<70% for CO_2 conversion at 300 °C using concentrated CO_2 and H_2) over Ru-based catalysts [43,56–57].

The mechanism of ICCM over Ru/CeO_2-MgO was studied by in situ DRIFTS characterization using Ru/rod-CeO_2-MgO catalyst with Ru/rod-CeO_2 as the benchmark, as shown in Fig. 9. During the CO_2 adsorption of Ru/CeO_2-MgO, a set of peaks appeared and gradually increased, including the peaks at 1614 cm^{-1} (bidentate carbonates [58]) and 1815 cm^{-1} (carbonyl vibration of carbonates), which represented the CO_2 adsorption on MgO by forming carbonates. The peaks belonging to CO_2 adsorption can be saturated within 15 mins over Ru/CeO_2-MgO combined materials. As for the key intermediates, we observed CO_2 dissociation at the initial time of CO_2 adsorption, including the peaks at 2037 cm^{-1} and 1993 cm^{-1} (linear or bridged Ru-CO [14,59–61]). The dissociation of CO_2 on Ru was fast and stable under Ar purge and vanished quickly under H_2. With the introduction of H_2, there is also a

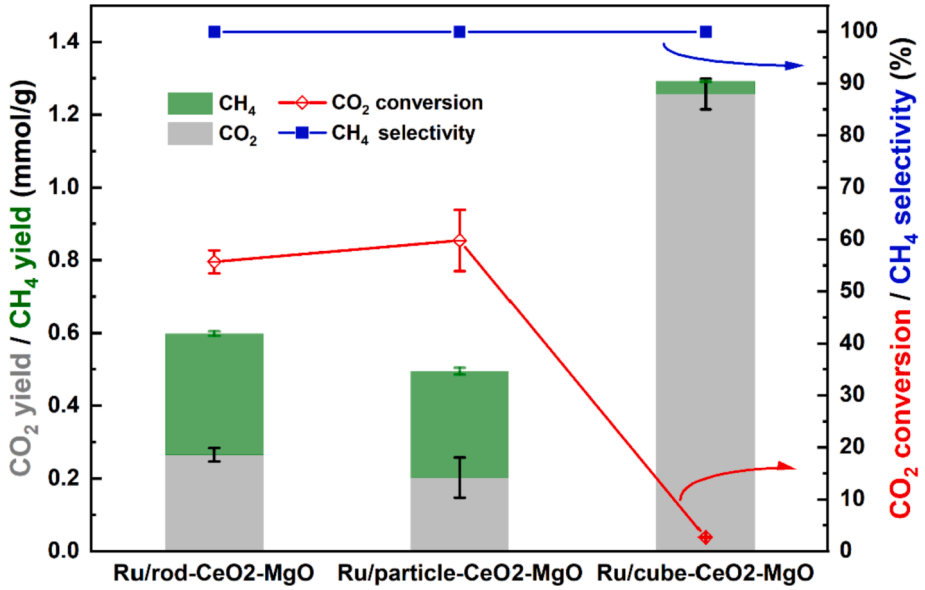

Fig. 6. ICCM performance over Ru/CeO_2-MgO with different CeO_2 morphologies. (Adsorbing in 100 ml min^{-1} 35% CO_2/N_2 at 300 °C for 1 h; purging in 50 ml min^{-1} N_2 for 10 min, reacting in 50 ml min^{-1} 5% H_2/N_2 at 300 °C.)

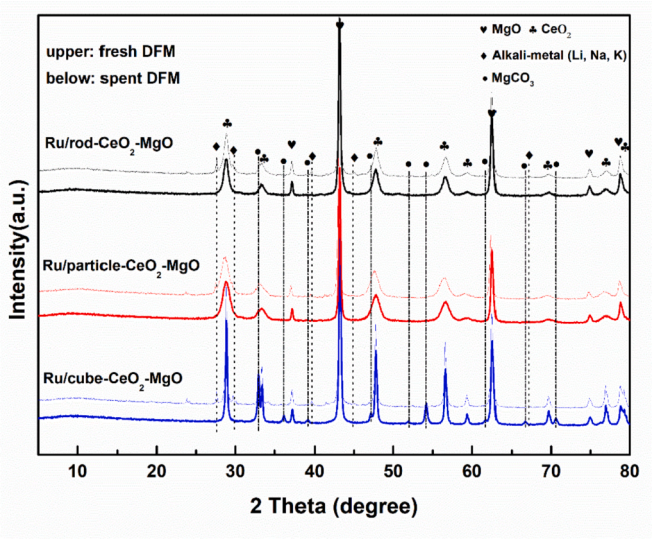

Fig. 7. XRD patterns of fresh and spent Ru/CeO_2-MgO catalysts.

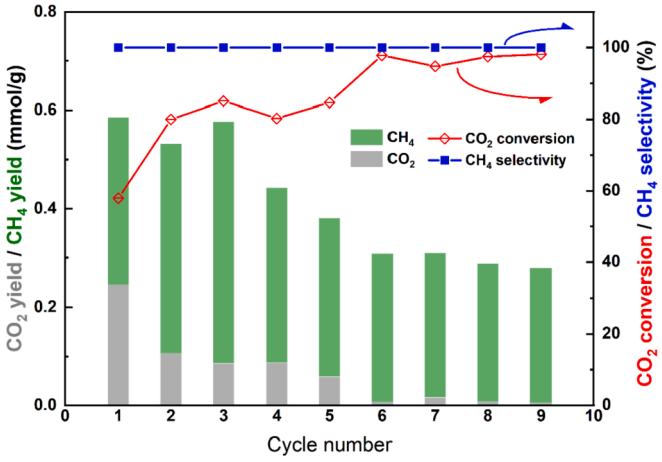

Fig. 8. ICCM cycle evaluation of Ru/rod-CeO_2-MgO combined materials.

significant peak shift from 1614 cm^{-1} to 1582 cm^{-1}(conjugated C-O/C = O of formats [14,61]) and OCO peak at 1367 cm-1 [62], representing the possible formates reaction pathway on the surface of $MgCO_3$. Ru/rod-CeO_2 can also adsorb CO_2 to form carbonates [63], which may be related to the oxygen vacancies on the surface. In short, there are mainly two reaction pathways in ICCM over Ru/CeO_2-MgO, including CO_2 dissociation on Ru and formates on $MgCO_3$. The gradually increased CO_2 conversion during cyclic ICCM over Ru/rod-CeO_2-MgO might be attributed to the promotion of the formates pathway.

Therefore, as illustrated in Fig. 10, it is suggested that (1) in the first step of CO_2 adsorption, MgO acts as the main adsorbent to form $MgCO_3$ while CeO_2 with oxygen vacancies can promote extra CO_2 adsorption by forming bicarbonates. (2) two reaction routes for the release and transformation of the adsorbed CO_2 under 5% H_2/N_2 atmosphere are proposed. Route 1 is the decomposition of $MgCO_3$ to release gas-phase CO_2 and then generate CH_4 with the assistance of H_2 and active sites by the CO_2 dissociation pathway. Route 2 is the reduction of carbonates (Eq. (6)) by the formates pathway. Route 2 does not rely on the gas phase CO_2 spillover and can achieve ideal ICCM performance, ~100% CO_2 conversion.

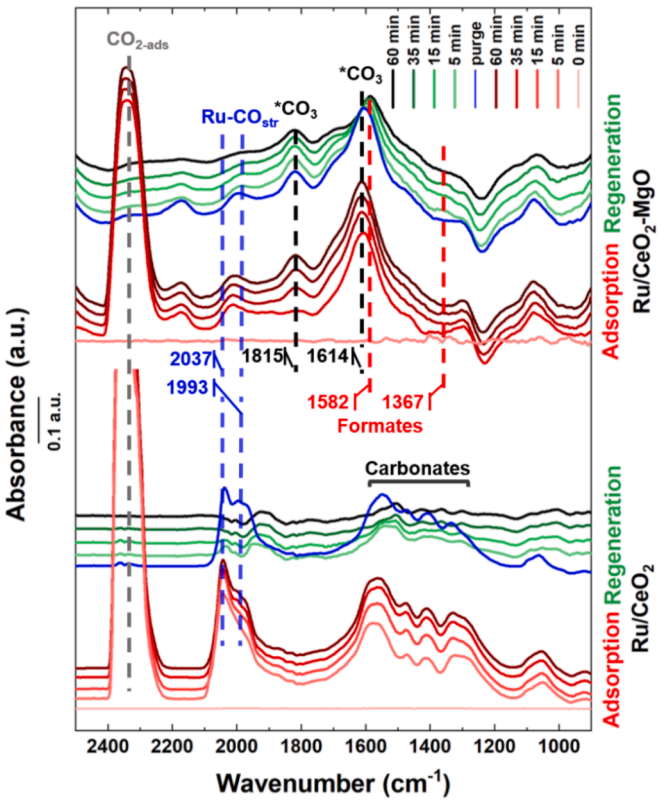

Fig. 9. In situ DRIFTS of ICCM over Ru/rod-CeO_2-MgO and Ru/rod-CeO_2.

4. Conclusion

An integrated CO_2 capture and methanation (ICCM) process has been performed using Ru/CeO_2-MgO combined materials with different CeO_2 morphologies, including rod, particle, and cube. In this ICCM process, CO_2 adsorption and in situ methanation are isothermally (300 °C) carried out over Ru/CeO_2-MgO combined materials in a single reactor. It is demonstrated that there are clear effects of support morphology on CO_2 conversion and CH_4 yield in ICCM. The results show that Ru/rod-CeO_2-MgO and Ru/particle-CeO_2-MgO exhibit significantly higher CH_4 yield (0.33 and 0.29 mmol/g_{DFM}) and CO_2 conversion (55.7% and 59.8%) compared with Ru/cube-CeO_2-MgO, yielding 0.03 mmol/g_{DFM} CH_4 with only 2.7% CO_2 conversion. The comprehensive characterizations of combined materials reveal that the rod-CeO_2 and particle-CeO_2 supported Ru possess higher surface area, better Ru dispersion and more abundant support-metal interactions, contributing to the enhanced ICCM performance. In addition, the oxygen vacancies on CeO_2 mainly enhance the CO_2 adsorption performance. Notably, the ICCM of Ru/rod-CeO_2-MgO shows stable CH_4 yield in cycles and can achieve > 95% CO_2 conversion after 5 cycles, showing significant superiority compared to traditional CO_2 methanation (<70% for CO_2 conversion under similar conditions).

The critical intermediates of ICCM were investigated to understand the mechanism of the whole process. In situ DRIFTS study indicates that ICCM over Ru/rod-CeO_2-MgO proceeds via the formates and CO_2 dissociation (Ru-CO species) pathways. The formates pathway do not require gas phase CO_2 to release from carbonates. Therefore, it could contribute to achieving ideal ICCM performance (100% CO_2 conversion and 100% CH_4 selectivity). Improving the formates pathway and inhibiting gas-phase CO_2 release in the methanation step could be a promising strategy to achieve perfect ICCM.

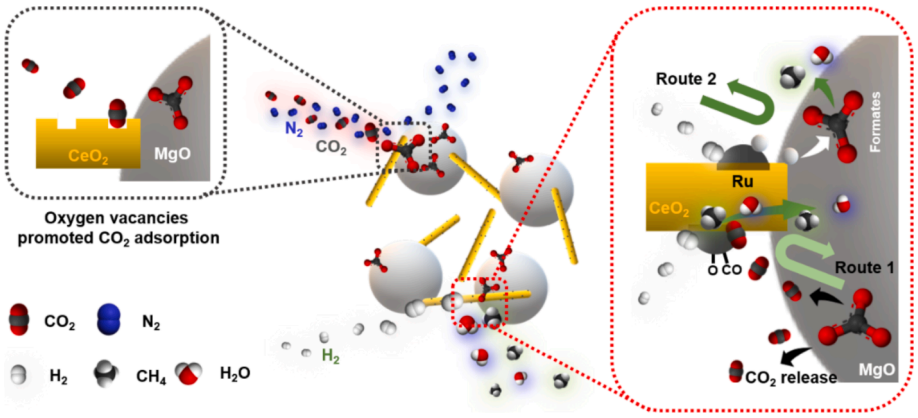

Fig. 10. Schematic diagram of ICCM over Ru/rod-CeO_2-MgO.

CRediT authorship contribution statement

Shuzhuang Sun: Methodology, Investigation, Resources, Data curation, Writing – original draft, Visualization. **Hongman Sun:** Conceptualization, Resources, Formal analysis. **Shaoliang Guan:** Resources. **Shaojun Xu:** Resources, Writing – review & editing, Supervision. **Chunfei Wu:** Writing – review & editing, Supervision, Project administration, Funding acquisition.

Declaration of Competing Interest

The authors declare that they have no known competing financial interests or personal relationships that could have appeared to influence the work reported in this paper.

Acknowledgement

Funding: The authors gratefully acknowledge financial support from the China Scholarship Council (reference number: 201906450023). This project has received funding from the European Union's Horizon 2020 research and innovation programme under the Marie Skłodowska-Curie grant agreement No. 823745.

We also acknowledge for the XPS data collection performed at the EPSRC National Facility for XPS ('HarwellXPS'), operated by Cardiff University and UCL, under contract No. PR16195. UK Catalysis Hub is kindly thanked for resources and support provided via our membership of the UK Catalysis Hub Consortium and funded by EPSRC grant: EP/R026939/1.

References

[1] Wang SJ, Li GD, Fang CL. Renew Sust Energy Rev 2018;81:2144–59.
[2] Wang QA, Luo JZ, Zhong ZY, Borgna A. Energy Environ Sci 2011;4:42–55.
[3] Wang F, He S, Chen H, Wang B, Zheng LR, Wei M, et al. J Am Chem Soc 2016;138:6298–305.
[4] Baysal Z, Kureti S. Appl Catal B Environ 2020:262.
[5] Yi N, Si R, Saltsburg H, Flytzani-Stephanopoulos M. Energy Environ Sci 2010;3:831–7.
[6] Kim DH, Park JL, Park EJ, Kim YD, Uhm S. ACS Catal 2014;4:3117–22.
[7] Porosoff MD, Yan B, Chen JG. Energy Environ Sci 2016;9:62–73.
[8] Barroso-Quiroga MM, Castro-Luna AE. Int J Hydrog Energy 2010;35:6052–6.
[9] Tian S, Yan F, Zhang Z, Jiang J. Sci Adv 2019;5:eaav5077.
[10] Sun H, Wang J, Zhao J, Shen B, Shi J, Huang J, et al. Appl Catal B Environ 2019;244:63–75.
[11] Duyar MS, Treviño MAA, Farrauto RJ. Appl Catal B Environ 2015;168–169:370–6.
[12] Kim SM, Abdala PM, Broda M, Hosseini D, Coperet C, Muller C. ACS Catal 2018;8:2815–23.
[13] Psarras PC, Comello S, Bains P, Charoensawadpong P, Reichelstein S, Wilcox J. Environ Sci Technol 2017;51:11440–9.
[14] Proano L, Tello E, Arellano-Trevino MA, Wang SX, Farrauto RJ, Cobo M. Appl Surf Sci 2019;479:25–30.
[15] Guo Y, Mei S, Yuan K, Wang DJ, Liu HC, Yan CH, et al. ACS Catal 2018;8:6203–15.
[16] Park JN, McFarland EW. J Catal 2009;266:92–7.
[17] Parastaev A, Muravev V, Osta EH, van Hoof AJ, Kimpel TF, Kosinov N, et al. Nat Catal 2020;3:526–33.
[18] Zhang XY, You R, Li D, Cao T, Huang WX. ACS Appl Mater Interfaces 2017;9:35897–907.
[19] Du XJ, Zhang DS, Shi LY, Gao RH, Zhang JP. J Phys Chem C 2012;116:10009–16.
[20] Zhan WC, He Q, Liu XF, Guo YL, Wang YQ, Wang L, et al. J Am Chem Soc 2016;138:16130–9.
[21] Tang HL, Su Y, Zhang BS, Lee AF, Isaacs MA, Wilson K, et al. Sci Adv 2017:3.
[22] Xu C, Qu XG. NPG Asia Mater 2014:6.
[23] Nie L, Mei DH, Xiong HF, Peng B, Ren ZB, Hernandez XIP, et al. Science 2017;358:1419-+.
[24] Aneggi E, Wiater D, de Leitenburg C, Llorca J, Trovarelli A. ACS Catal 2014;4:172–81.
[25] J. Paier, C. Penschke and J. Sauer, *Chem. Rev.*, 2013, **113**, 3949-2985.
[26] Gupta VK, Singh AK, Gupta B. Anal Chim Acta 2006;575:198–204.
[27] Slostowski C, Marre S, Dagault P, Babot O, Toupance T, Aymonier C. J CO_2 Util 2017;20:52–8.
[28] Ma ZW, Zhao SL, Pei XP, Xiong XM, Hu B. Catal Sci Technol 2017;7:191–9.
[29] Wang Z, Huang ZP, Brosnahan JT, Zhang S, Guo YL, Guo Y, et al. Environ Sci Technol 2019;53:5349–58.
[30] Li CW, Sun Y, Djerdj I, Voepel P, Sack CC, Weller T, et al. ACS Catal 2017;7:6453–63.
[31] Cargnello M, Doan-Nguyen VVT, Gordon TR, Diaz RE, Stach EA, Gorte RJ, et al. Science 2013;341:771–3.
[32] Li X, Lin J, Li L, Huang Y, Pan X, Collins SE, et al. Angew Chem Int Ed 2020;59:19983–9.
[33] Matsubu JC, Zhang S, DeRita L, Marinkovic NS, Chen JG, Graham GW, et al. Nat Chem 2017;9:120–7.
[34] He H, Yang P, Li J, Shi R, Chen L, Zhang A, et al. Ceram Int 2016;42:7810–8.
[35] Wu Q, Zhang F, Xiao P, Tao H, Wang X, Hu Z. J Phys Chem C 2008;112:17076–80.
[36] Mai H, Sun L, Zhang Y, Si R, Feng W, Zhang H, et al. J Phys Chem B 2005;109:24380–5.
[37] Li X, Han Y, Huang Y, Lin J, Pan X, Zhao Z, et al. Appl Catal B 2021;298:120597.
[38] Harada T, Simeon F, Hamad EZ, Hatton TA. Chem Mat 2015;27:1943–9.
[39] Sun H, Zhang Y, Guan S, Huang J, Wu C. J CO_2 Util 2020;38:262–72.
[40] Wang SX, Schrunk ET, Mahajan H, Farrauto RJ. Catalysts 2017:7.
[41] Bermejo-Lopez A, Pereda-Ayo B, Gonzalez-Marcos JA, Gonzalez-Velasco JR. Appl Catal B Environ 2019;256:11.
[42] Cimino S, Boccia F, Lisi L. J CO_2 Util 2020;37:195–203.
[43] Sakpal T, Lefferts L. J Catal 2018;367:171–80.
[44] Tana ML, Zhang J, Li HJ, Li YL, Shen WJ. Catal Today 2009;148:179–83.
[45] Okal J, Zawadzki M, Kraszkiewicz P, Adamska K. Appl Catal A Gen 2018;549:161–9.
[46] Hosokawa S, Kanai H, Utani K, Taniguchi Y-I, Saito Y, Imamura S. Appl Catal B Environ 2003;45:181–7.
[47] Hosokawa S, Taniguchi M, Utani K, Kanai H, Imamura S. Appl Catal A Gen 2005;289:115–20.
[48] Li JH, Liu ZQ, Cullen DA, Hu WH, Huang JE, Yao LB, et al. ACS Catal 2019;9:11088–103.
[49] Liu PC, Niu RY, Li W, Wang S, Li JP. Catal Lett 2019;149:1007–16.
[50] Huang H, Dai QG, Wang XY. Appl Catal B Environ 2014;158:96–105.
[51] Mittal M, Gupta A, Pandey O. Sol Energy 2018;165:206–16.
[52] Xie H, Wang H, Geng Q, Xing Z, Wang W, Chen J, et al. Inorg Chem 2019;58:5423–7.
[53] Zhao BR, Pan YX, Liu CJ. Catal Today 2012;194:60–4.
[54] Zhang Y, Liang L, Chen Z, Wen J, Zhong W, Zou S, et al. Appl Surf Sci 2020. https://doi.org/10.1016/j.apsusc.2020.146035, 146035.
[55] Liu K, Zhao X, Ren G, Yang T, Ren Y, Lee AF, et al. Nat Commun 2020;11:1–9.
[56] Petersen EM, Rao RG, Vance BC, Tessonnier J-P. Appl Catal B Environ 2021;286:119904.
[57] Abdel-Mageed AM, Wiese K, Parlinska-Wojtan M, Rabeah J, Bruckner A, Behm RJ. Appl Catal B Environ 2020;270:14.
[58] Hu G, Zhu L, Jia A, Hu X, Xie G, Lu J, et al. Appl Spectrosc 2012;66:122–7.

[59] Xu S, Chansai S, Xu S, Stere CE, Jiao Y, Yang S, et al. ACS Catal 2020;10:12828–40.
[60] Xu S, Chansai S, Stere C, Inceesungvorn B, Goguet A, Wangkawong K, et al. Nat Catal 2019;2:142–8.
[61] Cherevotan A, Raj J, Dheer L, Roy S, Sarkar S, Das R, et al. ACS Energy Lett 2021;6:509–16.
[62] Li CC, Liu XH, Lu GZ, Wang YQ. Chin J Catal 2014;35:1364–75.
[63] Wang F, Li C, Zhang X, Wei M, Evans DG, Duan X. J Catal 2015;329:177–86.